



HAL
open science

Heterostructured S-TiO₂ /g-C₃N₄ Photocatalysts with High Visible Light Photocatalytic Activity

Yassine Alaya, Bilel Chouchene, Ghouti Medjahdi, Lavinia Balan, Nouredine Bouguila, Raphaël Schneider

► **To cite this version:**

Yassine Alaya, Bilel Chouchene, Ghouti Medjahdi, Lavinia Balan, Nouredine Bouguila, et al.. Heterostructured S-TiO₂ /g-C₃N₄ Photocatalysts with High Visible Light Photocatalytic Activity. *Catalysts*, 2024, 14 (4), pp.226. 10.3390/catal14040226 . hal-04525027

HAL Id: hal-04525027

<https://hal.univ-lorraine.fr/hal-04525027>




Submitted on 28 Mar 2024

HAL is a multi-disciplinary open access archive for the deposit and dissemination of scientific research documents, whether they are published or not. The documents may come from teaching and research institutions in France or abroad, or from public or private research centers.

L'archive ouverte pluridisciplinaire **HAL**, est destinée au dépôt et à la diffusion de documents scientifiques de niveau recherche, publiés ou non, émanant des établissements d'enseignement et de recherche français ou étrangers, des laboratoires publics ou privés.

Article

Heterostructured S-TiO₂/g-C₃N₄ Photocatalysts with High Visible Light Photocatalytic Activity

Yassine Alaya ¹, Bilel Chouchene ², Ghouti Medjahdi ³, Lavinia Balan ⁴, Noureddine Bouguila ¹ and Raphaël Schneider ^{2,*}

¹ Laboratoire de Physique des Matériaux et des Nanomatériaux Appliquée à l'Environnement, Faculté des Sciences de Gabès, Gabès University, Gabès 6072, Tunisia; yassine1alaya@gmail.com (Y.A.); bouguila.nour@gmail.com (N.B.)

² Université de Lorraine, CNRS, LRGP, F-54000 Nancy, France; bilel.chouchene@univ-lorraine.fr

³ Université de Lorraine, CNRS, IJL, F-54000 Nancy, France; ghouti.medjahdi@univ-lorraine.fr

⁴ CEMHTI-UPR 3079 CNRS, Site Haute Température, 1D Avenue de la Recherche Scientifique, F-45071 Orléans, France; lavinia.balan@cnrs-orleans.fr

* Correspondence: raphael.schneider@univ-lorraine.fr; Tel.: +33-372743790

Abstract: Novel heterojunctions associating graphitic carbon nitride g-C₃N₄ and S-doped TiO₂ nanoparticles were successfully designed and prepared via a hydrothermal method and used for photocatalytic degradations. The loading in S-TiO₂ nanoparticles on g-C₃N₄ was varied (5, 10 and 20 wt%), and the photocatalysts were characterized by XRD, FT-IR, solid-state UV-visible diffuse reflectance, photoluminescence, XPS, TEM and SEM. The S-TiO₂ (5%)/g-C₃N₄ catalyst exhibits the highest activity for the photocatalytic degradation of the methylene blue (MB) dye under visible light irradiation. The high photocatalytic performance originates from the enhanced separation and transfer of photo-generated charge carriers. The S-TiO₂ (5%)/g-C₃N₄ photocatalyst is stable and can be reused five times without a sharp drop in activity, indicating its high potential for wastewater remediation.

Keywords: S-doped TiO₂; g-C₃N₄ nanohybrids; heterostructured photocatalysts; photocatalytic degradation



Citation: Alaya, Y.; Chouchene, B.; Medjahdi, G.; Balan, L.; Bouguila, N.; Schneider, R. Heterostructured S-TiO₂/g-C₃N₄ Photocatalysts with High Visible Light Photocatalytic Activity. *Catalysts* **2024**, *14*, 226. <https://doi.org/10.3390/catal14040226>

Academic Editor: Anna Kubacka

Received: 4 March 2024

Revised: 20 March 2024

Accepted: 26 March 2024

Published: 28 March 2024



Copyright: © 2024 by the authors. Licensee MDPI, Basel, Switzerland. This article is an open access article distributed under the terms and conditions of the Creative Commons Attribution (CC BY) license (<https://creativecommons.org/licenses/by/4.0/>).

1. Introduction

In recent years, various chemical, physical and biochemical processes including chlorination, Fenton reactions, coagulation, membrane separation or adsorption have been developed to treat wastewater and remove emerging pollutants like dyes and pigments, drugs, pesticides or heavy metals [1,2]. All these processes are not fully satisfactory because they require either powerful oxidants or only move pollutants from a liquid phase to a solid phase. Heterogeneous photocatalysis is an advanced oxidation process (AOP) and is considered as a valuable alternative to the treatments previously mentioned for wastewater treatment as it is environmentally friendly and requires only a light source and a catalyst for the degradation of harmful compounds present in water [3,4].

Upon light activation of a semiconductor photocatalyst, reactive oxygen species (ROS) like hydroxyl or superoxide radicals, singlet oxygen or hydrogen peroxide may be produced after oxidation of water molecules or reduction of molecular oxygen molecules adsorbed at the surface of the photocatalyst [4–6]. ROS exhibit strong oxidizing power, can fragment toxic organic molecules and, in the optimal conditions, mineralize them into CO₂ and H₂O. The choice of the photocatalyst and its ability to be photoactivated and produce ROS under illumination will therefore play a crucial role for the photodegradation of harmful compounds. One of the key points will be the inhibition of the charge carrier's recombination to improve their diffusion to the surface of the photocatalyst. Graphitic carbon nitride (g-C₃N₄) is one of the most studied photocatalysts in recent years due to its easy synthesis, low cost and good photocatalytic performance [6–10].

g-C₃N₄ is an organic semiconductor easily prepared by thermal polymerization of N-rich precursors such as melamine, urea or dicyandiamide and exhibits high thermal and chemical stability [6–10]. Moreover, the energy bandgap of g-C₃N₄ is of ca. 2.7 eV, which allows an improved utilization of solar light compared to wide bandgap metal oxides such as ZnO or TiO₂. However, the quantum efficiency of g-C₃N₄ is relatively modest due to the high recombination rate of photo-generated charge carriers. To overcome this limitation, many studies have focused on the construction of g-C₃N₄-based heterostructured photocatalysts [6,10–13]. The heterojunction can effectively decrease and even inhibit electron–hole pairs recombination thus enhancing their participation in reactions occurring at the surface of the photocatalyst (water oxidation and oxygen reduction to produce hydroxyl and superoxide radicals, respectively).

TiO₂ is one of the most used photocatalysts due to its high photoreactivity, high stability, low toxicity and low cost, and has very often been coupled with g-C₃N₄ to construct a heterojunction due to the matched energy band between these semiconductors [14]. The engineered g-C₃N₄/TiO₂ heterostructured photocatalysts were successfully used in various photocatalytic applications, such as pollutant degradation [15–24], organic synthesis [25], water splitting [15,26–28], CO₂ reduction [28,29] and NO_x oxidation [30].

The doping of TiO₂ with S is an effective method to narrow the bandgap and enhance the visible light photoactivity because the S atom has a lower electronegativity and higher 3p orbital energy than that of the O atom. The S dopants can substitute either O as an anion or Ti as a cation which allows for the introduction of additional extrinsic electronic levels located in the energy band gap of TiO₂ [31–33]. However, due to the high stability of TiO₂ and to the larger ionic radius of S than that of O, the S-doping of TiO₂ at an adequate concentration is usually difficult. To prepare S-doped TiO₂, the layered TiS₂ can be used as a precursor and oxidized in air at temperatures of 500–600 °C [34,35]. However, such high temperatures do not allow to maintain a high level of S doping in the TiO₂ crystal lattice [34]. S-doped TiO₂ can also be prepared via the hydrothermal oxidation of TiS₂ under acidic conditions [36,37].

Only three recent reports describe the synthesis of S-doped TiO₂ associated to g-C₃N₄. Biswal, Pany et al. prepared g-C₃N₄/S-doped TiO₂ particles by co-pyrolysis at 500 °C of TiOSO₄ and urea and further associated the composite to Ti₃C₂ to yield photocatalysts for water splitting [38,39]. Hossain et al. described the synthesis of S-doped TiO₂ by treatment of TiCl₄ with dye wastewater sludge followed by calcination at 600 °C. The produced S-doped TiO₂ was further associated to g-C₃N₄ by annealing with melamine at 550 °C and the obtained photocatalysts used for NO_x removal [40].

Herein, a mild hydrothermal process was developed for the preparation of anatase S-doped TiO₂ (S-TiO₂) containing ca. 11% S by hydrolysis of TiS₂ at neutral pH. When this hydrolysis was conducted in the presence of g-C₃N₄, S-TiO₂ nanoparticles with an average diameter of ca. 9.2 nm were found to be deposited on g-C₃N₄ sheets. The S-TiO₂/g-C₃N₄ heterojunction exhibits high photocatalytic activity and stability for the degradation of the methylene blue (MB) dye under visible light irradiation. Based on optical and electronic data, the enhanced photocatalytic activity of the S-TiO₂/g-C₃N₄ composite was demonstrated to originate from the enhanced visible light absorption and from the increased lifetime of photogenerated charge carriers.

2. Results

2.1. Synthesis and Characterization of S-TiO₂/g-C₃N₄ Catalysts

TiS₂ was prepared by reacting elemental S with TiCl₄ in 1-octadecene (ODE) at 300 °C [41]. The synthesis of S-TiO₂/g-C₃N₄ catalysts was performed by associating g-C₃N₄ with TiS₂ in water under sonication followed by a hydrothermal treatment at 160 °C for 4 h (Figure 1). This hydrothermal treatment allows a partial hydrolysis of TiS₂ into S-TiO₂ nanoparticles which are deposited on the surface of g-C₃N₄ sheets.

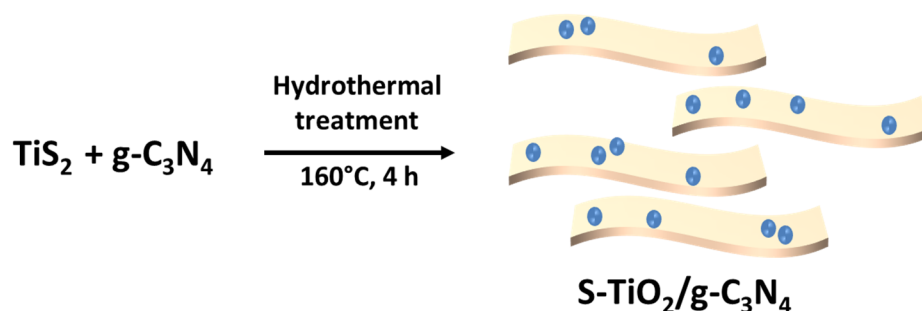


Figure 1. Schematic representation of the synthesis of S-TiO₂/g-C₃N₄ photocatalysts.

The crystallographic structure of the prepared catalysts was determined by X-ray diffraction (XRD) (Figure 2a). The XRD pattern of S-TiO₂ shows that all peaks correspond to the tetragonal crystalline structure of TiO₂ (anatase form, JCPDS No 01-071-1167). For g-C₃N₄, the signal at 13.03° is associated with the (100) the interlayer structural packing, while the signal at 27.56° corresponds to the (002) interplanar staking of aromatic systems [6,10]. The intensity of the g-C₃N₄ (100) peak is markedly reduced after association with S-TiO₂, indicating that the long-range order of the in-plane structural packing of g-C₃N₄ is altered likely due to the intralayer hydrogen bond breaking. A shift of the g-C₃N₄ (002) signal from 27.28° to 27.56° is also observed when increasing the loading in S-TiO₂ from 0 to 20 wt%, suggesting a distortion of the g-C₃N₄ layered structure after association with S-TiO₂ (Figure 2b). The interplanar distance decreases (0.3268, 0.3262, 0.3235 and 0.3230 nm for g-C₃N₄, S-TiO₂ (5%)/g-C₃N₄, S-TiO₂ (10%)/g-C₃N₄ and S-TiO₂ (20%)/g-C₃N₄, respectively), indicating a more compact packing of g-C₃N₄ sheets which should improve the charge carrier separation. These results confirm the successful association of S-TiO₂ with g-C₃N₄.

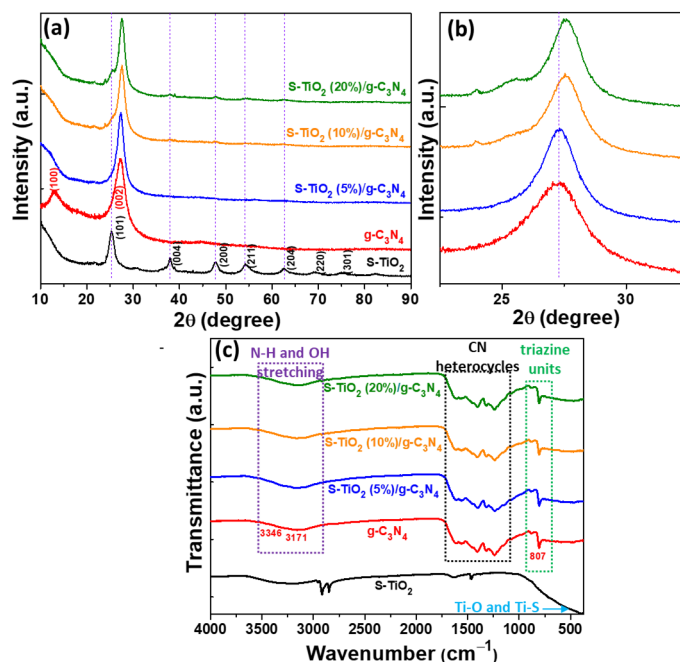


Figure 2. (a) XRD patterns, (b) magnification of the 22.5–32.5° zone and (c) FT-IR spectra of S-TiO₂, g-C₃N₄ and S-TiO₂/g-C₃N₄ photocatalysts.

The chemical structure of S-TiO₂ and S-TiO₂/g-C₃N₄ samples was further investigated by Fourier transform infrared spectroscopy (FT-IR) (Figure 2c). For S-TiO₂, the broad band located at 3500–3300 cm^{−1} originates from the O-H stretching vibration of chemisorbed water molecules. The O-H bending vibration can also be observed at 1630 cm^{−1}. The signals

observed at 2924 and 2856 cm^{-1} correspond to asymmetrical and symmetrical stretching vibrations of the C–H bonds, which suggests that ODE molecules used as solvent for the synthesis are still adsorbed on the surface of S-TiO₂ particles. The strong and broad band located in the 700–500 cm^{-1} range can be assigned to the Ti–O–Ti and Ti–S–Ti stretching vibrations [42]. For g-C₃N₄, the signals at 3346 and 3171 cm^{-1} correspond to the O–H stretching of adsorbed water molecules and to the N–H groups located at the periphery of g-C₃N₄ sheets, respectively. The stretching modes of C=N and C–N–C bonds in triazine heterocycles appear at 1621, 1545, 1456, 1398, 1314, and 1229 cm^{-1} while the sharp peak located at 803 cm^{-1} can be assigned to the out-of-plane breathing mode of triazine units in g-C₃N₄ [6,10]. All characteristic FT-IR signals of S-TiO₂ and g-C₃N₄ can be observed in g-C₃N₄/S-TiO₂ catalysts.

X-ray photoelectron spectroscopy (XPS) was further used to investigate the composition and the valence state of elements composing the S-TiO₂/g-C₃N₄ photocatalysts using the catalyst loaded with 5 wt% S-TiO₂ as representative. The XPS overview spectrum indicates the presence of C, N, O, S and Ti elements without impurity elements (Figure 3a). The N 1s signal can be deconvoluted into three peaks located at 398.62, 400.17 and 401.17 eV corresponding to bicoordinated N atoms (C=N=C bonds), bridging N atoms (N-(C)₃ bonds) and peripheral N atoms (NH₂ or NH bonds), respectively (Figure 3b) [6,10]. The signals observed at 404.50 eV is associated to the charging effects in heterocycles. The main signal observed at 288.81 eV in the HR-XPS spectrum of C 1s can be assigned to sp²-bonded carbon (N=C=N) bonds in aromatic units (Figure 3c) [6,10]. The signal observed at 284.81 eV originates from adventitious carbon. The weak signals observed at 286.31 eV and 288.61 eV correspond to carbon linked to one or two oxygen atoms, respectively, which suggests the presence of carbonyl or carboxyl groups on the edges of g-C₃N₄ sheets. The Ti 2p_{3/2} signal appears at 458.47 eV, value slightly lower than that of Ti(+4) in TiO₂ (458.70 eV), which confirms that S atoms are incorporated into the TiO₂ lattice which conducts to a shift to a lower binding energy (Figure 3d) [43]. The O 1s spectrum shows three signals at 529.91, 533.0 and 531.57 eV corresponding to O atoms in the TiO₂ lattice [42] and to O atoms engaged in C–OH and C=O bonds, respectively, indicating that g-C₃N₄ sheets are functionalized by oxygenated groups (Figure 3e) [44]. The major signal observed for S 2p_{3/2} is located at 163.14 eV, indicating that S in the –2 oxidation state is present in S-TiO₂ nanoparticles, which corresponds to Ti–S bonds in the TiO₂ lattice (Figure 3f) [42]. The weaker signal observed at 166.49 eV corresponds to S in the +4 oxidation state and could be assigned to oxidized S atoms in the form of O=S=O bonds in the TiO₂ lattice [45]. The XPS analysis also shows that TiO₂ particles are doped by approximately 11% S, which allows to propose the TiO_{1.78}S_{0.22} formula for these nanoparticles.

The microstructure and the morphology of g-C₃N₄, S-TiO₂ and S-TiO₂/g-C₃N₄ catalysts were characterized by scanning electron microscopy (SEM) and transmission electron microscopy (TEM). The SEM images of S-TiO₂ (5%)/g-C₃N₄ catalyst show that g-C₃N₄ is composed of auto-assembled thin sheets with an average size of ca. 150 nm (Figure 4a,b). g-C₃N₄ assemblies are porous, which is conducive to catalytic activity. The SEM image in chemical contrast allows to distinguish g-C₃N₄ from S-TiO₂ nanoparticles which appear as small aggregates deposited on the surface of g-C₃N₄ (Figure 4c). The SEM-associated energy dispersive X-ray (EDX) analysis confirms the presence of C, N, O, S and Ti elements (Figure 4d).

TEM images confirm the small size and the lamellar structure of g-C₃N₄ and the deposition of S-TiO₂ nanoparticles with an average size of ca. 9.2 ± 1.8 nm on the surface of g-C₃N₄ sheets (Figure 5a–c). The interplanar distances of 0.18 nm (200) and 0.35 nm (101) correlate well with the anatase structure of S-TiO₂ (Figure 5c). The elemental mapping confirms the presence of C, N, Ti, O and S elements and the presence of S-TiO₂ clusters of nanoparticles dispersed on g-C₃N₄, which is beneficial for the charge transfer between S-TiO₂ and g-C₃N₄ (Figure 5d–i). The chemical composition determined by the EDX analysis gives an atomic ratio of Ti/S of 8.44, indicating that the doping percentage of S in TiO₂ is of 11.8 (Figure 5j). This value is close to the doping percentage of 11% determined by XPS.

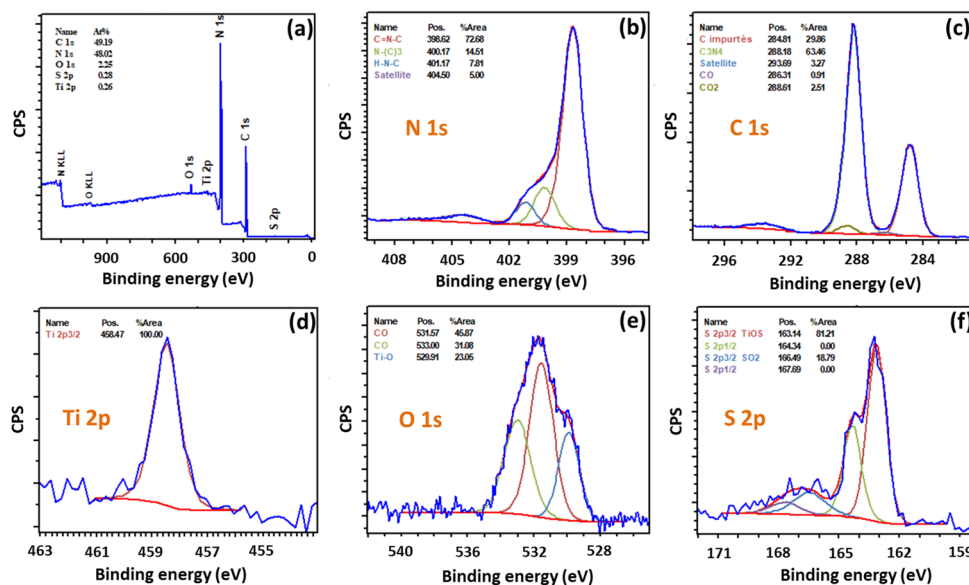


Figure 3. (a) Overview XPS spectrum of the S-TiO₂ (5%)/g-C₃N₄ sample and HR-XPS spectra of (b) N 1s, (c) C 1s, (d) Ti 2p, (e) O 1s and (f) S 2p.

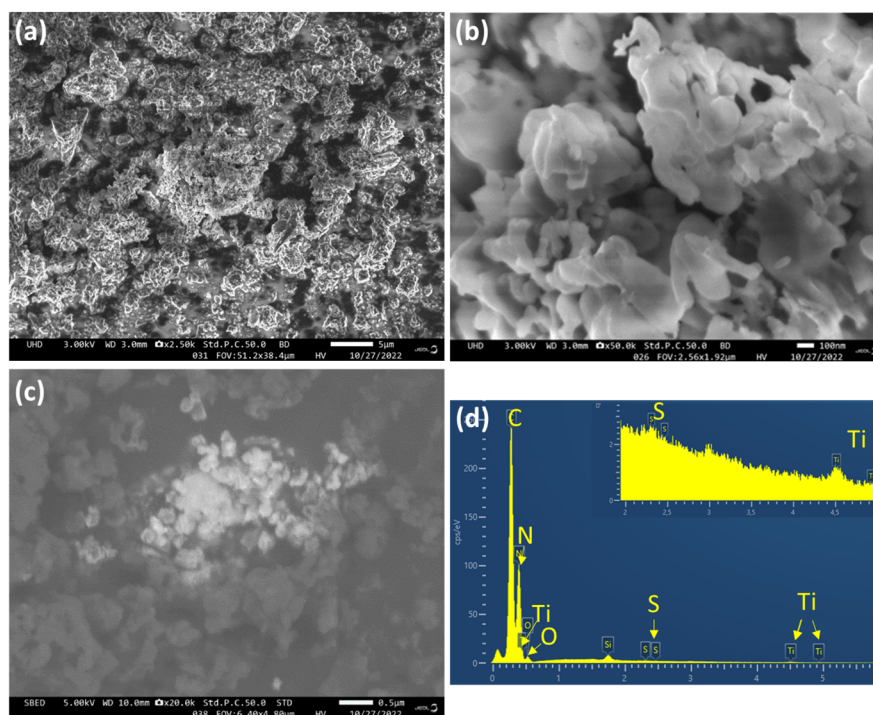


Figure 4. (a,b) SEM images of the S-TiO₂ (5%)/g-C₃N₄ catalyst, (c) SEM image in chemical contrast and (d) the SEM-associated EDX analysis.

Figure 6a shows the UV-visible diffuse reflectance spectra (DRS) of S-TiO₂, g-C₃N₄ and S-TiO₂/g-C₃N₄ catalysts recorded in the range 250–1000 nm. After association of S-TiO₂ with g-C₃N₄, the visible light absorption is increased compared to pure g-C₃N₄. The plots of $(\alpha h\nu)^{1/2}$ vs. photon energy (eV), where α , h and ν are the absorption coefficient, the Planck constant and the light frequency, respectively, were used to determine the bandgap energies S-TiO₂, g-C₃N₄ and S-TiO₂/g-C₃N₄ materials (Figure 6b). Pure S-TiO₂ and g-C₃N₄ exhibit bandgap energies of 3.09 and 2.80 eV, respectively. The decreased bandgap of S-TiO₂ compared to pure TiO₂ (E_g of 3.2 eV for pure anatase TiO₂) confirms the presence of S atoms in the crystal lattice, which agrees well with literature [46]. With the increase of

the S-TiO₂ loading in the photocatalysts, the bandgap gradually decreases from 2.80 to 2.75, 2.71, and 2.67 eV for g-C₃N₄ associated 5, 10 and 20% S-TiO₂, respectively. The increased light absorption in the visible range of S-TiO₂/g-C₃N₄ composites should be beneficial for the formation of charge carriers under visible light irradiation and thus increase the photocatalytic activity.

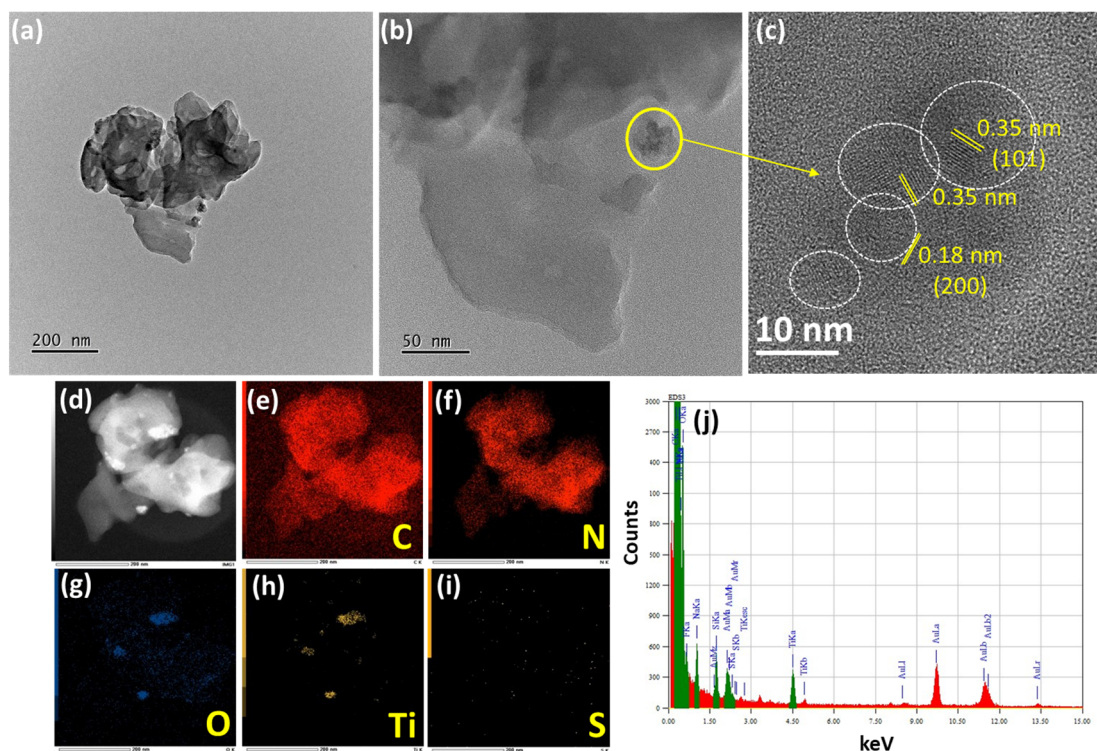


Figure 5. (a,b) TEM and (c) HR-TEM images, (d–i) elemental mapping and (j) EDX analysis of the S-TiO₂ (5%)/g-C₃N₄ material. The yellow circle corresponds to a cluster of S-TiO₂ particles and each white circle corresponds to a S-TiO₂ particle.

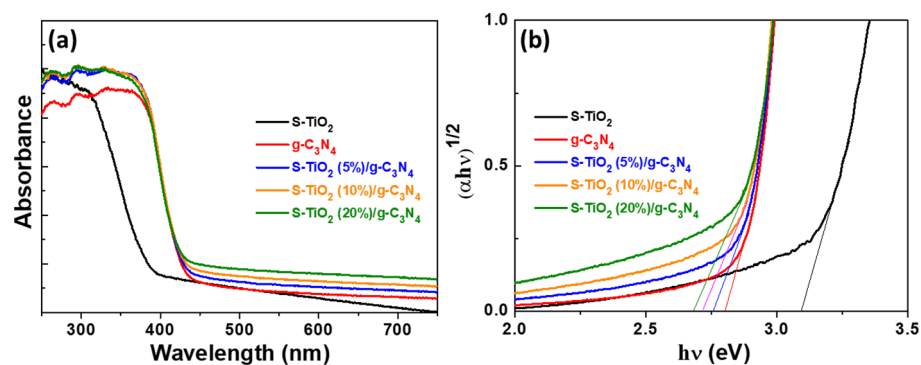


Figure 6. (a) UV-visible DRS of S-TiO₂, g-C₃N₄ and S-TiO₂/g-C₃N₄ catalysts and (b) plots of $[\alpha h\nu]^{1/2}$ vs. photon energy to determine the energy bandgap. The tangent of the linear portion of the curve was used to determine the bandgap energy.

The separation efficiency of photogenerated charge carriers was examined through PL measurements that provide valuable information on the separation and the lifetime of photogenerated electron–hole pairs (Figure 7) [6,10]. After excitation at 350 nm, g-C₃N₄ exhibits a strong PL emission centered at 433 nm while S-TiO₂ is non-fluorescent. The PL of S-TiO₂/g-C₃N₄ catalysts decreases gradually with the increase of the S-TiO₂ loading from 5 to 20 wt%. As the PL emission originates from the recombination of electron–hole pairs in g-C₃N₄, the decrease of the PL intensity observed after association with S-TiO₂

nanoparticles is indicative of an enhancement of the charge carriers lifetime originating from the charge transfer between g-C₃N₄ and S-TiO₂ nanoparticles.

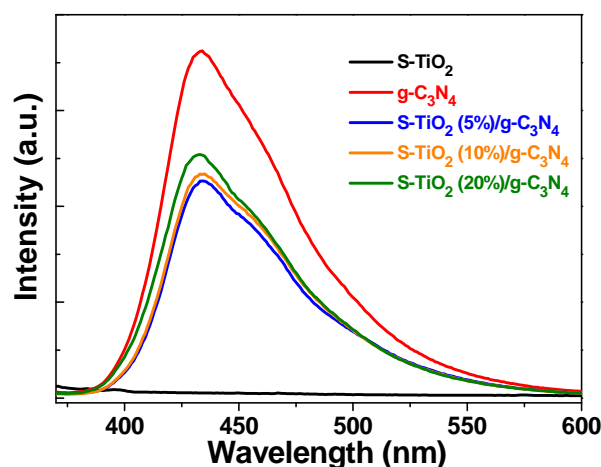


Figure 7. Room temperature PL emission spectra of S-TiO₂, g-C₃N₄ and S-TiO₂/g-C₃N₄ photocatalysts ($\lambda_{\text{ex}} = 350$ nm).

2.2. Photocatalytic Activity

The photocatalytic performance of S-TiO₂/g-C₃N₄ catalysts was evaluated in the degradation of the methylene blue (MB) dye under visible light irradiation (intensity of 30 mW/cm²) and at room temperature. MB was chosen as model dye as it is present in colored aqueous effluents from textile industries. MB is also a carcinogenic pollutant and its negative impact on both humans and aquatic life is well known. A control experiment showed that less than 4% of the dye was bleached in these experimental conditions without the photocatalyst. The adsorption–desorption equilibrium between the photocatalyst and MB molecules was reached by stirring in the dark for 60 min prior to irradiation. Figure 8a shows that the S-TiO₂ (5%)/g-C₃N₄ composite exhibits the highest photodegradation rate of MB under visible light (quantitative photodegradation after 240 min irradiation). Further increase of S-TiO₂ content in the photocatalyst (10 and 20 wt%) decreases the photocatalytic activity of the composite catalysts likely due to the blocking of g-C₃N₄ active sites by S-TiO₂ nanoparticles deposited on their surface and/or to the enhanced photogenerated charges recombination. These photocatalytic results are in good accordance with PL measurements.

The obtained kinetic data could be fitted by a first-order kinetic model, $\ln(C_0/C) = kt$, where C_0 is the initial concentration of MB, C is the MB concentration at time t and k is the apparent pseudo-first-order rate constant (Figure 8b). The apparent first-order rate constants k were determined from the slope of the $\ln(C_0/C)$ vs. irradiation time curves and were found to be 0.0057, 0.0207, 0.0194 and 0.0107 min⁻¹ for g-C₃N₄ and S-TiO₂/g-C₃N₄ catalysts containing 5, 10 and 20 wt% S-TiO₂, respectively, further confirming that the g-C₃N₄/S-TiO₂ (5%) catalyst exhibits the highest activity.

The monitoring of the UV-visible absorption of the MB solution during its photocatalytic degradation using the S-TiO₂ (5%)/g-C₃N₄ catalyst shows the decrease of the characteristic UV-visible absorption signal of MB at 664 nm (Figure 8c). The blue shift observed for the absorption peak of MB (from 664 to 625 nm) originates from the *N*-demethylation of the dye [47].

The stability and the reusability of the photocatalyst are crucial, especially for practical applications. The S-TiO₂ (5%)/g-C₃N₄ catalyst was used for the photodegradation of MB in five cycles under visible light irradiation. After each run, the catalyst was recovered by centrifugation and reused without any treatment. As shown in Figure 8d, only a small decrease in photocatalytic performance is observed after each cycle (from 100 to 85% after the fifth cycle). The weak decrease in photocatalytic activity could be related to the adsorption of by-products from MB photodegradation as the catalyst was not washed or

dried between two cycles. These results show not only that the catalyst is stable but also of interest for real environmental applications.

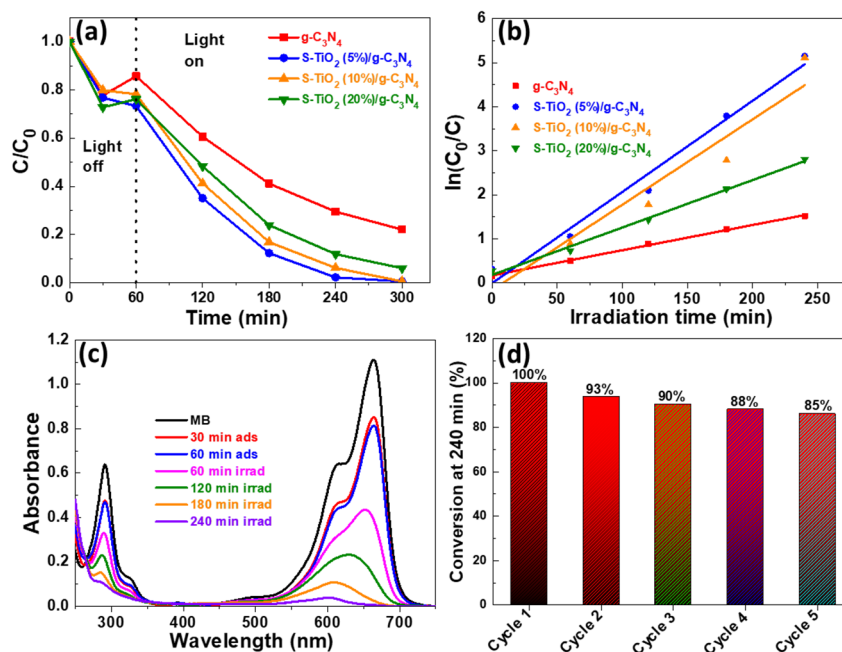


Figure 8. (a) Photocatalytic performances of $g\text{-C}_3\text{N}_4$, and $\text{S-TiO}_2/g\text{-C}_3\text{N}_4$ catalysts for the degradation of MB, (b) plots of $\ln(C_0/C)$ vs. irradiation time, (c) UV-visible spectral changes of MB during its photodegradation by the S-TiO_2 (5%)/ $g\text{-C}_3\text{N}_4$ catalyst under visible light irradiation (intensity $30\text{ mW}/\text{cm}^2$). (d) Recycling runs of the S-TiO_2 (5%)/ $g\text{-C}_3\text{N}_4$ photocatalyst.

Figure 9a shows the influence of the catalyst loading (15, 30 or 45 mg of S-TiO_2 (5%)/ $g\text{-C}_3\text{N}_4$ in 30 mL of BM) was also investigated. With low catalyst load (15 mg in 30 mL of MB solution), MB photodegradation is slow ($k = 0.0063\text{ min}^{-1}$) and incomplete after 240 min irradiation. The highest photodegradation rate was reached using 30 mg of catalyst in 30 mL of the MB solution ($k = 0.0207\text{ min}^{-1}$). A decrease of the photodegradation rate is observed when the catalyst loading was increased to 45 mg in 30 mL of the MB solution likely due to light scattering and screening effects ($k = 0.0129\text{ min}^{-1}$) [48].

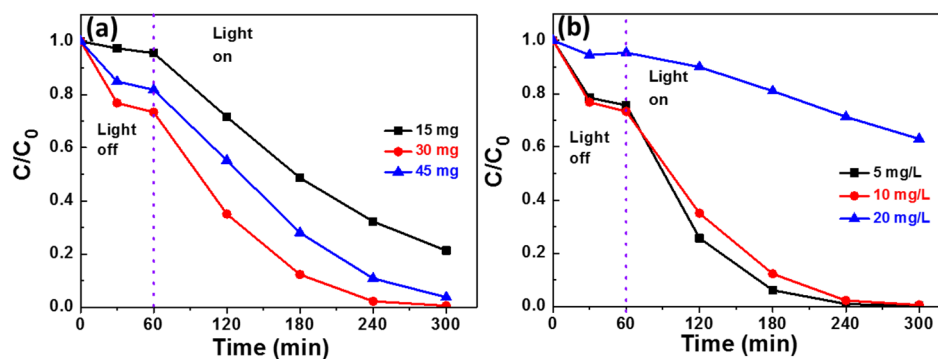


Figure 9. Influence of (a) the S-TiO_2 (5%)/ $g\text{-C}_3\text{N}_4$ catalyst loading on MB photodegradation, and (b) influence of MB concentration on the photodegradation rate.

The influence of the MB concentration (5, 10 or 20 mg/L) on the photodegradation rate was also studied (Figure 9b). Similar results were obtained for MB concentrations of 5 and 10 mg/L ($k = 0.0267$ and 0.0207 min^{-1} for concentrations of MB of 5 and 10 mg/L, respectively), indicating that the surface of the catalyst is not saturated by MB molecules adsorbed on its surface and that the production of reactive species responsible for MB pho-

todegradation is not hindered. However, at a concentration of 20 mg/L, the degradation rate decreased markedly ($k = 0.0019 \text{ min}^{-1}$), suggesting that the catalyst surface is saturated by MB or by intermediates generated from MB photocatalytic degradation.

The surface charge of the photocatalyst has a very important role on the photocatalytic performance because it does not only influence the adsorption of pollutants as well as that of photodegradation intermediates on the catalyst surface but also the nature of the reactive species produced for the photodegradation [49]. Figure 10a shows the surface Zeta potential vs. pH of $g\text{-C}_3\text{N}_4$ and S-TiO_2 (5%)/ $g\text{-C}_3\text{N}_4$ catalysts. The pH of the point of charge (pzc) of $g\text{-C}_3\text{N}_4$ is 4.7, which agrees with previous reports [6,10]. A slight increase of the pzc to 5.6 is observed upon association with S-TiO_2 particles as the pzc of TiO_2 is of ca. 7.5 [50]. In this context, the influence of the pH of the MB solution on the photocatalytic degradation was also investigated (Figure 10b). The pH of the MB solution was adjusted from 2 to 11 using 0.1 M HCl or NaOH before the photocatalytic experiment. The adsorption of MB at the surface of the catalyst is weak (ca. 10–15%) at pH 2 and 4 due to the electrostatic repulsion between the catalyst and the dye, both positively charged. As the pH further increases, the adsorption is more marked (up to 85% at pH 11) because the charge of the catalyst becomes more and more negative. For pH values between 5 and 9, the photodegradation of MB requires approximately 180 min of irradiation to be complete. At pH 11, approximately 85% of the dye is adsorbed to the catalyst surface after 60 min in the dark and the remaining MB in solution is decomposed in 60 min. The FT-IR analysis of the photocatalyst after reaction shows that a high proportion of MB is not degraded but simply adsorbed. The k values are the highest for pH values ranging from 5 to 9 ($k = 0.0207, 0.0239$ and 0.0265 min^{-1} at pH 5, 7 and 9, respectively).

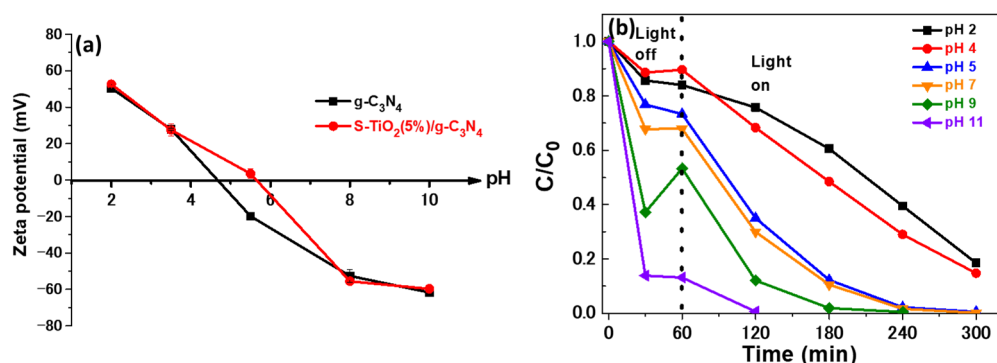


Figure 10. (a) Zeta potential of $g\text{-C}_3\text{N}_4$ and S-TiO_2 (5%)/ $g\text{-C}_3\text{N}_4$ catalysts vs. pH. (b) Influence of pH on the photocatalytic degradation of MB using the S-TiO_2 (5%)/ $g\text{-C}_3\text{N}_4$ catalyst.

The photocatalytic performances of the S-TiO_2 (5%)/ $g\text{-C}_3\text{N}_4$ catalyst were compared to those of recently developed heterostructured $\text{TiO}_2/g\text{-C}_3\text{N}_4$ photocatalysts for MB degradation (Table 1). Even if it is difficult to compare the performances because the quantities of catalyst, the concentration in MB or the irradiation conditions are not identical, the S-TiO_2 (5%)/ $g\text{-C}_3\text{N}_4$ catalyst is one of the most effective for the degradation of MB under visible irradiation.

2.3. Reaction Mechanism

To investigate the photocatalytic degradation mechanism, trapping experiments were conducted to identify the active species produced by the S-TiO_2 (5%)/ $g\text{-C}_3\text{N}_4$ catalyst at neutral pH. Tert-butanol (t-BuOH), DMSO, ammonium oxalate (AO), TEMPOL and NaN_3 were used as hydroxyl $\bullet\text{OH}$ radicals, electrons (e^-), holes (h^+), superoxide $\text{O}_2^{\bullet-}$ radicals and singlet oxygen $^1\text{O}_2$ scavengers, respectively. The percentage of MB photodegradation was estimated by UV-visible spectroscopy after 240 min visible light irradiation. As shown in Figure 11a, the addition of DMSO or TEMPOL causes a decrease in photodegradation, indicating that electrons (e^-) and superoxide $\text{O}_2^{\bullet-}$ radicals are involved in the photodegradation mechanism. Holes play the major role on the photodegradation as the largest

decrease in photocatalytic activity is observed after addition of AO. Other scavengers have only a minor influence on photodegradation.

Table 1. Photocatalytic performance of recently developed heterostructured catalysts used for the degradation of MB.

Photocatalyst	Photocatalyst Amount (g/L)	[MB] (mg/L)	Light Source	Removal (%)	Reaction Time (min)	Ref
g-C ₃ N ₄ /TiO ₂	Immobilized catalyst	10	Visible light	97.6	240	[51]
g-C ₃ N ₄ /TiO ₂	0.1	10	Solar light illumination	80	180	[52]
TiO ₂ /g-C ₃ N ₄	Not provided	5	Simulated sunlight	84.6	120	[53]
g-C ₃ N ₄ /TiO ₂ -ZnO	1	10	Visible light	62.4	120	[54]
Sm-doped TiO ₂ /g-C ₃ N ₄	1	1000	Visible light	91.8	120	[55]
TiO ₂ /g-C ₃ N ₄	0.2	10	Visible light	100	70	[56]
B-doped g-C ₃ N ₄ /TiO ₂	1	Not provided	Visible light	81	225	[57]
g-C ₃ N ₄ /TiO ₂	0.2	30	Simulated sunlight	100	120	[58]
GO/g-C ₃ N ₄ /TiO ₂	0.1	10	Visible light	98.8	240	[59]
TiO ₂ /g-C ₃ N ₄	0.3	10	Simulated sunlight	100	60	[60]
g-C ₃ N ₄ /TiO ₂	0.4	20	Visible light	96.6	60	[61]
S-doped TiO ₂ /g-C ₃ N ₄	1	10	Visible light	100	240	This work

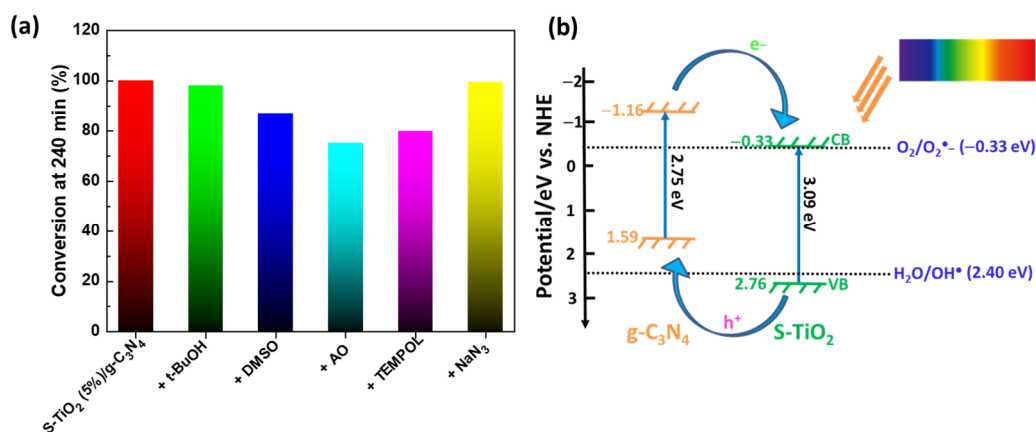


Figure 11. (a) Influence of scavengers of $\bullet\text{OH}$ radicals, electrons, holes, $\text{O}_2\bullet^-$ radicals and $^1\text{O}_2$ on the photocatalytic degradation of MB using the S-TiO₂ (5%)/g-C₃N₄ catalyst under visible light irradiation. All scavengers were used at a 10 mM concentration. (b) Schematic representation of the band diagram of the g-S-TiO₂ (5%)/g-C₃N₄ photocatalyst, of the charge transfer and of the redox potentials of $\text{O}_2/\text{O}_2\bullet^-$ and $\text{H}_2\text{O}/\bullet\text{OH}$ couples.

The band edge positions of S-TiO₂ and g-C₃N₄ were determined using Equations (1) and (2):

$$E_{\text{VB}} = \chi - E^e + 0.5 E_{\text{g}} \quad (1)$$

$$E_{\text{CB}} = E_{\text{VB}} - E_{\text{g}} \quad (2)$$

where E_{CB} and E_{VB} are the edge potentials of the conduction band (CB) and of the valence band (VB), respectively, χ is the Mulliken absolute electronegativity of the semiconductor ($\chi(\text{g-C}_3\text{N}_4) = 4.72 \text{ eV}$ and $\chi(\text{S-TiO}_2) = 5.72 \text{ eV}$ using the $\text{TiO}_{1.78}\text{S}_{0.22}$ formula determined by XPS) [62], E_{g} is the bandgap energy determined from UV-visible DRS, and E^e is the energy of free electrons on the hydrogen scale (ca. 4.5 eV). The determined E_{CB} and E_{VB} values for g-C₃N₄ are -1.16 and 1.59 eV vs. NHE, respectively, and E_{CB} and E_{VB} values for S-TiO₂ are -0.33 and 2.76 eV vs. NHE, respectively, which allows us to propose the energy diagram described in Figure 11b. The following Type II heterojunction mechanism for the S-TiO₂ (5%)/g-C₃N₄ catalyst can be proposed. Both semiconductors are photoactive under visible irradiation. Electrons photogenerated in the conduction band of g-C₃N₄ can either react

with adsorbed O_2 molecules to produce $O_2^{\bullet-}$ radicals that were demonstrated to play an important role in the photocatalytic degradation or be transferred to the conduction band of S-TiO₂ due to a mixed phases junction where the reduction of O_2 into $O_2^{\bullet-}$ can also take place. Simultaneously, the holes generated in the valence band of S-TiO₂ under light illumination are transferred to the valence band of g-C₃N₄. As holes play a key role in the photocatalytic mechanism, they likely oxidize MB into [MB]⁺. These mutual transfers of electrons and holes allowed by the construction of the Type II heterojunction reduce the probability of electron–hole pair recombination and favor the production of the reactive species responsible for the photocatalytic degradation of MB.

3. Materials and Methods

3.1. Reagents

Titanium tetrachloride TiCl₄ (99.9%, Merck, Darmstadt, Germany), sulfur S (99.98%, Merck), 1-octadecene ODE (90%, Fischer, Rider Increis, Austria), melamine (99%, Fischer), cyanuric chloride (98%, Fischer), methylene blue MB (Merck), *tert*-butanol *t*-BuOH (>99%, Merck), 4-hydroxy-2,2,6,6-tetramethylpiperidine 1-oxyl TEMPOL (95%, Merck), ammonium oxalate OA (99.5%, Fischer), DMSO (99.9%, Fischer), sodium azide NaN₃ (99%, Fischer), acetone (Carlo Erba, Cornaredo, Italy), methanol (VWR, Atlanta, GA, USA), ethanol (VWR) and toluene (Carlo Erba) were used as received.

3.2. Preparation of TiS₂

TiS₂ was prepared according to ref. [41] with slight modifications. Briefly, elemental sulfur (30 mmol) was added to 50 mL of ODE and the reaction flask was purged with argon and heated to 300 °C. Next, titanium tetrachloride (5 mmol) was injected and the reaction mixture was maintained at 300 °C for 30 min. After cooling to room temperature, the black precipitate produced was filtered and washed using acetone (30 mL) and a combination of methanol, toluene and acetone (2 × 30 mL) to remove any residual organic solvent and any by-products that may have formed during the reaction.

3.3. Synthesis of g-C₃N₄

Melamine (20 mmol) and cyanuric chloride (13.5 mmol) were solubilized in 20 mL of a THF/water (1/1) solution and the mixture was stirred at room temperature for 5 h until a white colored gel is obtained. The gel was dried in an oven at 60 °C for 12 h before being placed in a crucible with a lid and calcined for 1 h at 250 °C, 1 h at 350 °C, and 1 h at 450 °C to obtain bulk g-C₃N₄. After natural cooling, the powder was recovered and used without further treatment.

3.4. Preparation of S-TiO₂/g-C₃N₄ Photocatalysts

The S-TiO₂/g-C₃N₄ catalysts were prepared by impregnating g-C₃N₄ (250 mg) dispersed by sonication in 30 mL of water with TiS₂ (5, 10, and 20 wt%). The mixture was first ultrasonicated for 30 min, transferred into a stainless-steel autoclave and heated at 160 °C for 4 h. Finally, after natural cooling to room temperature, the S-TiO₂/g-C₃N₄ catalyst was washed with deionized water (4 × 20 mL) and dried at 70 °C for 15 h.

3.5. Photocatalytic Tests

The photodegradation of methylene blue (MB) used at a 10 mg/L concentration was investigated by using S-TiO₂/g-C₃N₄ photocatalysts under visible light irradiation (irradiance of 30 mW/cm²). Photodegradations were conducted in a batch reactor at 20 °C. Typically, the S-TiO₂/g-C₃N₄ catalyst (30 mg) was dispersed under sonication in 30 mL of the MB solution and the mixture was stirred in the dark in order to achieve adsorption-desorption equilibrium. After 60 min, the suspension was illuminated. Aliquots (1 mL) were taken from the solution at regular time intervals, centrifuged (4000 rpm for 5 min) to separate the catalyst and the concentration of MB in the supernatant was monitored by UV-visible absorption spectroscopy at 664 nm.

To identify the species involved in the photocatalytic degradation of MB, DMSO, *t*-BuOH, NaN₃, TEMPOL and AO were used to scavenge electrons, hydroxyl •OH radicals, singlet oxygen ¹O₂, superoxide O₂^{•−} radicals and holes, respectively. The experimental procedure is similar to that described above, except that scavengers were added at a 10 mM concentration.

3.6. Characterization

XRD analyses were performed on a Panalytical (Tokyo, Japan) X'Pert pro-MPD diffractometer with Cu Kα radiation in the 2θ range from 20° to 90°. The structure and the size of the photocatalysts were characterized by SEM (JEOL (Tokyo, Japan) JSM-6490 LV and JEOL JSM IT800 instruments coupled with EDS) and TEM (Philips (Amsterdam, The Netherlands) CM200 equipment). SAED images were obtained using the Philips CM200 equipment. The functional groups and the valence states of elements composing the S-TiO₂/g-C₃N₄ catalysts were investigated by XPS (Gammadata (Uppsala, Sweden) Scienta SES 200-2 spectrometer) and by FT-IR (ALPHA Bruker (Billerica, MA, USA) Optik spectrometer). The zeta potential of the catalysts was determined using a Malvern (Malvern, UK) Zetasizer Nano ZS instrument. UV-visible absorption spectra in liquid phase were recorded on a Thermo Scientific (Waltham, MA, USA) Evolution 220 spectrometer. UV-visible DRS of the catalysts were recorded using a Shimadzu (Kyoto City, Japan) 2600–2700 spectrometer with BaSO₄ as reference. The separation of charge carriers was investigated by PL using a Horiba (Kyoto City, Japan) Fluoromax-4 Jobin Yvon spectrofluorimeter.

4. Conclusions

In summary, a cheap and efficient hydrothermal method was developed for the preparation of new heterostructured photocatalysts associating S-TiO₂ and g-C₃N₄. TEM and XPS analyses show that S-TiO₂ particles with an average diameter of ca. 9.2 nm and doped with 11% S were deposited on g-C₃N₄ sheets. The photocatalytic performance was evaluated in the degradation of the MB dye under visible light irradiation. With the optimum loading of 5 wt% S-TiO₂, the S-TiO₂/g-C₃N₄ heterostructured photocatalyst exhibits high and stable photocatalytic activity. Scavenging experiments show that holes and superoxide radicals play a major role in the photodegradation of dye and that the heterojunction between g-C₃N₄ and S-TiO₂ is of Type II. The enhanced spatial separation of photo-generated electron–hole pairs account for the high photocatalytic activity of the S-TiO₂ (5%)/g-C₃N₄ catalyst.

Author Contributions: Conceptualization, N.B. and R.S.; methodology, Y.A. and B.C.; validation, R.S.; formal analysis, Y.A. and B.C.; investigation, Y.A., B.C., G.M. and L.B.; data curation, Y.A., B.C., G.M. and L.B.; writing—original draft preparation, Y.A. and B.C.; writing—review and editing, R.S.; supervision, N.B. and R.S.; project administration, R.S.; funding acquisition, R.S. All authors have read and agreed to the published version of the manuscript.

Funding: This research received no external funding.

Data Availability Statement: The data presented in this study are available on request from the corresponding author.

Acknowledgments: The authors are grateful to the expertise and the facilities of the Platform MACLE-CVL, co-funded by the European Union and Centre-Val de Loire Region (FEDER). The authors also acknowledge thank Khalid Ferji (LCPM, Université de Lorraine) for Zeta potential analyses.

Conflicts of Interest: The authors declare no conflicts of interest.

References

1. Rashid, R.; Shafiq, I.; Akhter, P.; Javid Iqbal, M.; Hussain, M. A state-of-the-art review on wastewater treatment techniques: The effectiveness of adsorption method. *Environ. Sci. Pollut. Res.* **2021**, *28*, 9050–9066. [[CrossRef](#)] [[PubMed](#)]
2. Dutta, D.; Arya, S.; Kumar, S. Industrial wastewater treatment: Current trends, bottlenecks, and best practices. *Chemosphere* **2021**, *285*, 131245. [[CrossRef](#)] [[PubMed](#)]
3. Adisurya Ismail, G.; Sakai, H. Review on effect of different type of dyes on advanced oxidation processes (AOPs) for textile color removal. *Chemosphere* **2022**, *291*, 132906. [[CrossRef](#)] [[PubMed](#)]

4. Dong, C.; Fang, W.; Yi, Q.; Zhang, J. A comprehensive review on reactive oxygen species (ROS) in advanced oxidation processes (AOPs). *Chemosphere* **2022**, *308*, 136205. [[CrossRef](#)]
5. Moussa, H.; Giroto, E.; Mozet, K.; Alem, H.; Medjahdi, G.; Schneider, R. ZnO rods/reduced graphene oxide composites prepared via a solvothermal reaction for efficient sunlight-driven photocatalysis. *Appl. Catal. B Environ.* **2016**, *185*, 11–21. [[CrossRef](#)]
6. Moussa, H.; Chouchene, B.; Gries, T.; Balan, L.; Mozet, K.; Medjahdi, G.; Schneider, R. Growth of ZnO Nanorods on Graphitic Carbon Nitride gCN Sheets for the Preparation of Photocatalysts with High Visible-Light Activity. *ChemCatChem* **2018**, *10*, 4987–4997. [[CrossRef](#)]
7. Wang, J.; Wang, S. A critical review on graphitic carbon nitride (g-C₃N₄)-based materials: Preparation, modification and environmental application. *Coord. Chem. Rev.* **2022**, *453*, 214338. [[CrossRef](#)]
8. Ismael, M. A review on graphitic carbon nitride (g-C₃N₄) based nanocomposites: Synthesis, categories, and their application in photocatalysis. *J. Alloys Compd.* **2020**, *846*, 156446. [[CrossRef](#)]
9. Zhang, M.; Yang, Y.; An, X.; Hou, L.-a. A critical review of g-C₃N₄-based photocatalytic membrane for water purification. *Chem. Eng. J.* **2021**, *412*, 128663. [[CrossRef](#)]
10. Ouedraogo, S.; Chouchene, B.; Desmarests, C.; Gries, T.; Balan, L.; Fournet, R.; Medjahdi, G.; Bayo, K.; Schneider, R. Copper octacarboxyphthalocyanine as sensitizer of graphitic carbon nitride for efficient dye degradation under visible light irradiation. *Appl. Catal. A Gen.* **2018**, *563*, 127–136. [[CrossRef](#)]
11. Zhu, B.; Cheng, B.; Fan, J.; Ho, W.; Yu, J. g-C₃N₄-Based 2D/2D Composite Heterojunction Photocatalyst. *Small Struct.* **2021**, *2*, 2100086. [[CrossRef](#)]
12. Li, Y.; Zhou, M.; Cheng, B.; Shao, Y. Recent advances in g-C₃N₄-based heterojunction photocatalysts. *J. Mater. Sci. Technol.* **2020**, *56*, 1–17. [[CrossRef](#)]
13. Chouchene, B.; Gries, T.; Balan, L.; Medjahdi, G.; Schneider, R. Graphitic carbon nitride/SmFeO₃ composite Z-scheme photocatalyst with high visible light activity. *Nanotechnology* **2020**, *31*, 465704. [[CrossRef](#)]
14. Acharya, R.; Parida, K. A review on TiO₂/g-C₃N₄ visible-light-responsive photocatalysts for sustainable energy generation and environmental remediation. *J. Environ. Chem. Eng.* **2020**, *8*, 103896. [[CrossRef](#)]
15. Tatykayev, B.; Chouchene, B.; Balan, L.; Gries, T.; Medjahdi, G.; Giroto, E.; Uralbekov, B.; Schneider, R. Heterostructured g-CN/TiO₂ Photocatalysts Prepared by Thermolysis of g-CN/MIL-125(Ti) Composites for Efficient Pollutant Degradation and Hydrogen Production. *Nanomaterials* **2020**, *10*, 1387. [[CrossRef](#)] [[PubMed](#)]
16. Shen, X.; Song, L.; Luo, L.; Zhang, Y.; Zhu, B.; Liu, J.; Chen, Z.; Zhang, L. Preparation of TiO₂/C₃N₄ heterojunctions on carbon-fiber cloth as efficient filter-membrane-shaped photocatalyst for removing various pollutants from the flowing wastewater. *J. Colloid Interface Sci.* **2018**, *532*, 798–807. [[CrossRef](#)]
17. Kane, A.; Chafiq, L.; Dalhatou, S.; Bonnet, P.; Nasr, M.; Gaillard, N.; Dangwang Dikdim, J.M.; Monier, G.; Amine Assadi, A.; Zeghioud, H. g-C₃N₄/TiO₂ S-scheme heterojunction photocatalyst with enhanced photocatalytic Carbamazepine degradation and mineralization. *J. Photochem. Photobiol. A Chem.* **2022**, *430*, 113971. [[CrossRef](#)]
18. Zhang, B.; He, X.; Ma, X.; Chen, Q.; Liu, G.; Zhou, Y.; Ma, D.; Cui, C.; Ma, J.; Xin, Y. In situ synthesis of ultrafine TiO₂ nanoparticles modified g-C₃N₄ heterojunction photocatalyst with enhanced photocatalytic activity. *Sep. Purif. Technol.* **2020**, *247*, 116932. [[CrossRef](#)]
19. Hu, K.; Li, R.; Ye, C.; Wang, A.; Wei, W.; Hu, D.; Qiu, R.; Yan, K. Facile synthesis of Z-scheme composite of TiO₂ nanorod/g-C₃N₄ nanosheet efficient for photocatalytic degradation of ciprofloxacin. *J. Clean. Prod.* **2020**, *253*, 120055. [[CrossRef](#)]
20. Hao, R.; Wang, G.; Tang, H.; Sun, L.; Xu, C.; Han, D. Template-free preparation of macro/mesoporous g-C₃N₄/TiO₂ heterojunction photocatalysts with enhanced visible light photocatalytic activity. *Appl. Catal. B Environ.* **2016**, *187*, 47–58. [[CrossRef](#)]
21. Wang, W.; Liu, Y.; Qu, J.; Chen, Y.; Tad, M.O.; Shao, Z. Synthesis of Hierarchical TiO₂-C₃N₄ Hybrid Microspheres with Enhanced Photocatalytic and Photovoltaic Activities by Maximizing the Synergistic Effect. *ChemPhotoChem* **2017**, *1*, 35–45. [[CrossRef](#)]
22. Cao, Y.; Yuan, G.; Guo, Y.; Hu, X.; Fang, G.; Wang, S. Facile synthesis of TiO₂/g-C₃N₄ nanosheet heterojunctions for efficient photocatalytic degradation of tartrazine under simulated sunlight. *Appl. Surf. Sci.* **2022**, *600*, 154169. [[CrossRef](#)]
23. Ni, S.; Fu, Z.; Li, L.; Ma, M.; Liu, Y. Step-scheme heterojunction g-C₃N₄/TiO₂ for efficient photocatalytic degradation of tetracycline hydrochloride under UV light. *Colloids Surf. A Physicochem. Eng.* **2022**, *649*, 129475. [[CrossRef](#)]
24. Liu, X.; Chen, N.; Li, Y.; Deng, D.; Xing, X.; Wang, Y. A general nonaqueous sol-gel route to g-C₃N₄-coupling photocatalysts: The case of Z-scheme g-C₃N₄/TiO₂ with enhanced photodegradation toward RhB under visible-light. *Sci. Rep.* **2016**, *6*, 39531. [[CrossRef](#)] [[PubMed](#)]
25. Zhang, Y.; Xu, J.; Mei, J.; Sarina, S.; Wu, Z.; Liao, T.; Yan, C.; Suna, Z. Strongly interfacial-coupled 2D-2D TiO₂/g-C₃N₄ heterostructure for enhanced visible-light induced synthesis and conversion. *J. Hazard. Mater.* **2020**, *394*, 122529. [[CrossRef](#)] [[PubMed](#)]
26. Jiang, Y.; Sun, Z.; Chen, Q.; Cao, C.; Zhao, Y.; Yang, W.; Zeng, L.; Huang, L. Fabrication of 0D/2D TiO₂ Nanodots/g-C₃N₄ S-scheme heterojunction photocatalyst for efficient photocatalytic overall water splitting. *Appl. Surf. Sci.* **2022**, *571*, 151287. [[CrossRef](#)]
27. Yang, J.; Wu, X.; Mei, Z.; Zhou, S.; Su, Y.; Wang, G. CVD Assisted Synthesis of Macro/Mesoporous TiO₂/g-C₃N₄ S-Scheme Heterojunction for Enhanced Photocatalytic Hydrogen Evolution. *Adv. Sustain. Syst.* **2022**, *6*, 220005. [[CrossRef](#)]
28. Zhang, X.; Ping Jiang, S. Layered g-C₃N₄/TiO₂ nanocomposites for efficient photocatalytic water splitting and CO₂ reduction: A review. *Mater. Today Energy* **2022**, *23*, 100904. [[CrossRef](#)]

29. Reli, M.; Huo, P.; Sihor, M.; Ambrozova, N.; Troppova, I.; Matejova, L.; Lang, J.; Svoboda, L.; Kustrowski, P.; Ritz, M.; et al. Novel TiO₂/C₃N₄ Photocatalysts for Photocatalytic Reduction of CO₂ and for Photocatalytic Decomposition of N₂O. *J. Phys. Chem. A* **2016**, *120*, 8564–8573. [[CrossRef](#)]
30. Mukit Hossain, S.; Park, H.; Kang, H.-J.; Seok Mun, J.; Tijing, L.; Rhee, I.; Kim, J.-H.; Jun, Y.-S.; Kyong Shon, H. Modified Hydrothermal Route for Synthesis of Photoactive Anatase TiO₂/g-CN Nanotubes from Sludge Generated TiO₂. *Catalysts* **2020**, *10*, 1350. [[CrossRef](#)]
31. Chen, X.; Burda, C. The Electronic Origin of the Visible-Light Absorption Properties of C-, N- and S-Doped TiO₂ Nanomaterials. *J. Am. Chem. Soc.* **2008**, *130*, 5018–5019. [[CrossRef](#)]
32. Tachikawa, T.; Tojo, S.; Kawai, K.; Endo, M.; Fujitsuka, M.; Ohno, T.; Nishijima, K.; Miyamoto, Z.; Majima, T. Photocatalytic oxidation reactivity of holes in the sulfur and carbon-doped TiO₂ powders studied by time-resolved diffuse reflectance spectroscopy. *J. Phys. Chem. B* **2004**, *108*, 19299–19306. [[CrossRef](#)]
33. Ohno, T.; Mitsui, T.; Matsumura, M. Photocatalytic Activity of S-doped TiO₂ Photocatalyst under Visible Light. *Chem. Lett.* **2003**, *32*, 364–365. [[CrossRef](#)]
34. Umabayashi, T.; Yamaki, T.; Itoh, H.; Asai, K. Band gap narrowing of titanium dioxide by sulfur doping. *Appl. Phys. Lett.* **2002**, *81*, 454. [[CrossRef](#)]
35. Umabayashi, T.; Yamaki, T.; Tanaka, S.; Asai, K. Visible Light-Induced Degradation of Methylene Blue on S-doped TiO₂. *Chem. Lett.* **2003**, *32*, 330–331. [[CrossRef](#)]
36. Ho, W.; Yu, J.C.; Lee, S. Low-temperature hydrothermal synthesis of S-doped TiO₂ with visible light photocatalytic activity. *J. Solid State Chem.* **2006**, *179*, 1171–1176. [[CrossRef](#)]
37. Lin, Y.-C.; Chien, T.-E.; Lai, P.-C.; Chiang, Y.-H.; Li, K.-L.; Lin, J.-L. TiS₂ transformation into S-doped and N-doped TiO₂ with visible-light catalytic activity. *Appl. Surf. Sci.* **2015**, *359*, 1–6. [[CrossRef](#)]
38. Pany, S.K.; Parida, M. A facile in situ approach to fabricate N,S-TiO₂/g-C₃N₄ nanocomposite with excellent activity for visible light induced water splitting for hydrogen evolution. *Phys. Chem. Chem. Phys.* **2015**, *17*, 8070–8077. [[CrossRef](#)] [[PubMed](#)]
39. Biswal, L.; Nayak, S.; Parida, K. Rationally designed Ti₃C₂/N,S-TiO₂/g-C₃N₄ ternary heterostructure with spatial charge separation for enhanced photocatalytic hydrogen evolution. *J. Colloid Interface Sci.* **2022**, *621*, 254–266. [[CrossRef](#)]
40. Mukit Hossain, S.; Park, H.; Kang, H.-J.; Seok Mun, J.; Tijing, L.; Rhee, I.; Kim, J.-H.; Jun, Y.-S.; Kyong Shon, H. Synthesis and NO_x removal performance of anatase S-TiO₂/g-CN heterojunction formed from dye wastewater sludge. *Chemosphere* **2021**, *275*, 130020. [[CrossRef](#)]
41. Lopez, J.; Gonzalez, R.; Ayala, J.; Cantu, J.; Castillo, A.; Parsons, J.; Myers, J.; Lodge, T.P.; Alcoutlabi, M. Centrifugally spun TiO₂/C composite fibers prepared from TiS₂/PAN precursor fibers as binder-free anodes for LIBS. *J. Phys. Chem. Solids* **2021**, *149*, 109795. [[CrossRef](#)]
42. Yang, G.; Yanb, Z.; Xiao, T. Low-temperature solvothermal synthesis of visible-light-responsive S-doped TiO₂ nanocrystal. *Appl. Surf. Sci.* **2012**, *258*, 4016–4022. [[CrossRef](#)]
43. Yang, J.; Bai, H.; Tan, X.; Lian, J. IR and XPS investigation of visible-light photocatalysis-Nitrogen-carbon-doped TiO₂ film. *Appl. Surf. Sci.* **2006**, *253*, 1988–1994. [[CrossRef](#)]
44. She, X.; Liu, L.; Ji, H.; Mo, Z.; Li, Y.; Huang, L.; Du, D.; Xu, H.; Li, H. Template-free synthesis of 2D porous ultrathin nonmetal-doped g-C₃N₄ nanosheets with highly efficient photocatalytic H₂ evolution from water under visible light. *Appl. Catal. B Environ.* **2016**, *187*, 144–153. [[CrossRef](#)]
45. Chen, X.; Glans, P.-A.; Qiu, X.; Dayal, S.; Jennings, W.D.; Smith, K.E.; Burda, C.; Guo, J. X-Ray Spectroscopic Study of the Electronic Structure of Visible-light Responsive N-, C- and S-Doped TiO₂. *J. Electron Spectrosc. Relat. Phenom.* **2008**, *162*, 67–73. [[CrossRef](#)]
46. McManamon, C.; O'Connell, J.; Delaney, P.; Rasappa, S.; Holmes, J.D.; Morris, M.A. A facile route to synthesis of S-doped TiO₂ nanoparticles for photocatalytic activity. *J. Mol. Catal. A Chem.* **2015**, *406*, 51–57. [[CrossRef](#)]
47. Zhang, T.; Oyama, T.; Aoshima, A.; Hidaka, H.; Zhao, J.; Serpone, N. Photooxidative N-demethylation of methylene blue in aqueous TiO₂ dispersions under UV irradiation. *J. Photochem. Photobiol. Chem.* **2001**, *140*, 163–172. [[CrossRef](#)]
48. Matos, J.; Laine, J.; Herrmann, J.-M. Synergy effect in the photocatalytic degradation of phenol on a suspended mixture of titania and activated carbon. *Appl. Catal. B Environ.* **1998**, *18*, 281–291. [[CrossRef](#)]
49. Ahmed, S.; Rasul, M.G.; Brown, R.; Hashib, M.A. Influence of parameters on the heterogeneous photocatalytic degradation of pesticides and phenolic contaminants in wastewater: A short review. *J. Environ. Manag.* **2011**, *92*, 311–330. [[CrossRef](#)]
50. Fernández-Nieves, A.; De las Nieves, F.J.; Richter, C. *Trends in Colloid and Interface Science XII*; Steinkopff: Dresden, Germany, 1998; pp. 21–24.
51. Xiuling, G.; Jihai, D.; Chaojie, L.; Zisheng, Z.; Weiwen, W. Fabrication of g-C₃N₄/TiO₂ photocatalysts with a special bilayer structure for visible light photocatalytic application. *Colloids Surf. A Physicochem. Eng. Asp.* **2020**, *599*, 124931.
52. Pelin, G.; Jongee, P.; Abdullah, Ö. Preparation and photocatalytic activity of g-C₃N₄/TiO₂ heterojunctions under solar light illumination. *Ceram. Int.* **2020**, *46*, 21431–21438.
53. Yarabahally, R.G.; Udayabhanu; Gubran, A.; Abdo, H.; Mysore, B.N.; Ganganagappa, N.; Kullaiiah, B. Facile and rapid synthesis of solar-driven TiO₂/g-C₃N₄ heterostructure photocatalysts for enhanced photocatalytic activity. *J. Sci. Adv. Mater. Devices* **2022**, *7*, 100419.
54. Sepide, S.; Bahram, K.; Zohreh, B. Synthesis and characterization of a g-C₃N₄/TiO₂-ZnO nanostructure for photocatalytic degradation of methylene blue. *Nano Futures* **2022**, *6*, 035001.

55. Tianyi, C.; Yuan, Z.; Yumin, Y.; Jianbo, Z.; Kezhen, Q.; Jianhui, J. Synthesis and properties of Sm-TiO₂ coupled with g-C₃N₄ for improved photocatalytic degradation toward methylene blue and tetracycline under visible-light irradiation. *Appl. Organomet. Chem.* **2022**, *36*, e6626.
56. Dang, T.N.H.; Nguyen, T.T.T.; Huynh, Q.A.T.; Le Van, T.S.; Le Vu, T.S.; Nguyen, D.V.Q.; Le Lam, S.; Tran, N.T.; Pham, L.M.T.; Ly, H.D.; et al. TiO₂/g-C₃N₄ Visible-Light-Driven Photocatalyst for Methylene Blue Decomposition. *J. Nanomater.* **2023**, *2023*, 9967890.
57. Sadia, F.; Umair, A.; Muhammad, B.T.; Wahid, A.; Muhammad, A.; Muhammad, S. Spinach derived boron-doped g-C₃N₄/TiO₂ composites for efficient photo-degradation of methylene blue dye. *Chemosphere* **2023**, *320*, 138002.
58. Vijayan, M.; Manikandan, V.; Rajkumar, C.; Hatamleh, A.A.; Alnafisi, B.K.; Easwaran, G.; Liu, X.; Sivakumar, K.; Kim, H. Constructing Z-scheme g-C₃N₄/TiO₂ heterostructure for promoting degradation of the hazardous dye pollutants. *Chemosphere* **2023**, *311*, 136928. [[CrossRef](#)]
59. Xiaoting, R.; Mingshuai, G.; Lili, X.; Likun, X.; Li, L.; Lehui, Y.; Min, W.; Yonglei, X.; Fangyuan, D.; Yadi, W. Photoelectrochemical performance and S-scheme mechanism of ternary GO/g-C₃N₄/TiO₂ heterojunction photocatalyst for photocatalytic antibiosis and dye degradation under visible light. *Appl. Surf. Sci.* **2023**, *630*, 157446.
60. Shuhua, L.; Xinxin, S.; Ying, W.; Boyang, J.; Caixia, S.; Debao, W. Construction of coordination bond electron bridge boosting interfacial electron transfer to enhance bifunctional photocatalytic activity of TiO₂/g-C₃N₄ heterojunction. *Mater. Today Commun.* **2023**, *37*, 107605.
61. Jiayi, W.; Penggang, R.; Yanli, D.; Xueyan, Z.; Zhengyan, C.; Lu, P.; Yanling, J. Construction of tubular g-C₃N₄/TiO₂ S-scheme photocatalyst for high-efficiency degradation of organic pollutants under visible light. *J. Alloys Compd.* **2023**, *947*, 169659.
62. Xu, Y.; Schoonen, M.A.A. The absolute energy positions of conduction and valence bands of selected semiconducting minerals. *Am. Mineral.* **2000**, *85*, 543–556. [[CrossRef](#)]

Disclaimer/Publisher's Note: The statements, opinions and data contained in all publications are solely those of the individual author(s) and contributor(s) and not of MDPI and/or the editor(s). MDPI and/or the editor(s) disclaim responsibility for any injury to people or property resulting from any ideas, methods, instructions or products referred to in the content.